Granular Matter (2006) 8: 159–174
DOI 10.1007/s10035-006-0004-4

ORIGINAL PAPER

Gian Antonio D'Addetta · Ekkehard Ramm

A microstructure-based simulation environment on the basis of an interface enhanced particle model

Received: 22 May 2005 / Published online: 3 March 2006

Abstract The present contribution introduces enhanced discrete element simulation methodologies (DEM) with a special focus on a microstructure-based model environment. Therewith, it is possible to represent the failure of cohesive granular materials like concrete, ceramics or marl in a qualitative as well as quantitative manner. Starting from a basic polygonal two-dimensional particle model for non-cohesive granular materials, more complex models for cohesive materials are obtained by inclusion of beam or interface elements between corresponding particles. In particular, we will introduce an interface enhanced DEM methodology where a standard ingredient of computational mechanics, namely interface elements, are combined with the particle methodology contained in the DEM. The last step in the series of increasing complexity is the realization of a microstructure-based simulation environment which utilizes the interface enhanced DEM methodology. With growing model complexity a wide variety of failure features of cohesive as well as non-cohesive geomaterials can be represented. Finally, the plan of the paper is enriched by the validation of the newly introduced and re-developed discrete models with regard to qualitative and quantitative aspects.

Keywords Particle model · Discrete element method · Lattice model · Interface model · Geomaterial · Cohesive frictional material · Microstructure

1 Introduction

From a physical point of view geomaterials like concrete, ceramics or marl can be considered as cemented granulates forming a heterogeneous macroscopic solid. In order to predict the remaining load capacity after reaching the ultimate load a substantiated knowledge of the underlying failure mechanisms is essential. Thereby, this knowledge may – for example – be based on micromechanical observations. The failure mechanisms of these materials are characterized by complex failure modes and, furthermore, they show a highly anisotropic bias due to their inhomogeneous microstructure. The growth and coalescence of microcracks in cohesive geomaterials lead to the formation of macroscopic crack patterns. Finally, this results in a fragmentation into separate particle clusters forming a solid-granulates mix. Behaving quasi-brittle under load these materials are characterized by a localization of deformations in narrow zones. Since localization phenomena like cracks or shear bands occur, the material cannot be treated as continuous in the usual manner. If fracture and fragmentation of the solid occurs, the creation and continuous motion of the evolving crack surfaces apparently represent discontinuous phenomena and are difficult to handle. Therefore, most continuum models, and in particular those ones based on continuum damage mechanics, cannot account for the discrete nature of material failure in a natural way and need some extension, confer [3,29,37]. Alternatively, discrete particle models like discrete element methods (DEM) have been developed. As the name DEM suggests, a solid is replaced by a discontinuous particle composite which allows for a detachment of bonds between particles (if initially present) and a re-contact of open surfaces. In order to simulate and quantify the full range of geomaterials from non-cohesive ones like sand to cohesive ones like concrete, ceramics or rock, starting from the pioneering work by [7] different types of discrete element models have been elaborated, see [6] for a recent review. Starting with a basic polygonal two-dimensional DEM model for non-cohesive granular materials, more complex models for cohesive materials are obtained by inclusion of beam or interface elements between corresponding particles. As the quantification of previously presented beam enhanced DEM models is an arduous task, see [10,11,20,21,22], the standard (non-cohesive) version of the DEM model, see [36], is augmented by interface elements between the particle edges. The formulation and numerical implementation of this interface enhanced DEM model will be presented in

G. A. D'Addetta(✉) · E. Ramm
Institute of Structural Mechanics, University of Stuttgart,
Pfaffenwaldring 7, 70550 Stuttgart, Germany
E-mail: gian-antonio.daddetta@gmx.de
Tel.: +49-711-6856123
Fax: +49-711-6856130

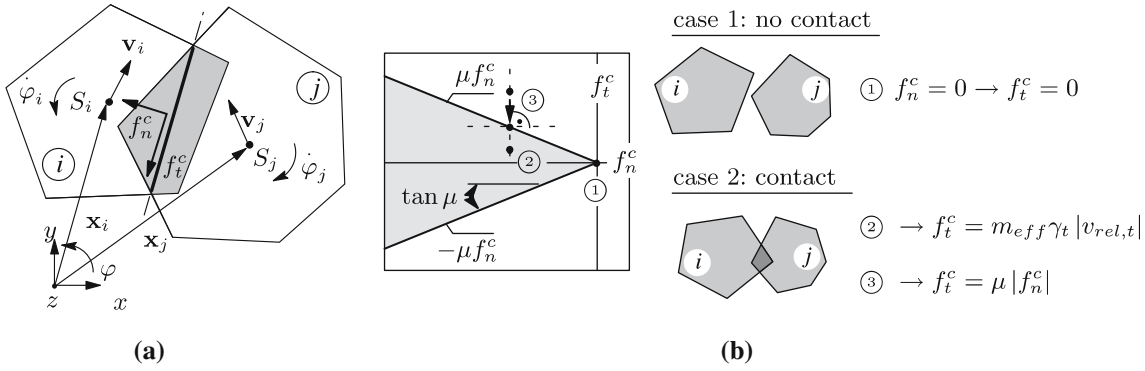

Fig. 1 **a** Geometry of the contact. **b** Interpretation of contact force logic in terms of plasticity law

detail in this paper. Thereby, tension and compression simulations of cohesive rectangular particle composites are utilized to validate the model. The next step is the realization of a microstructure-based simulation environment which utilizes the foregoing enhanced DEM models, confer [8]. The microstructure can be included, if different properties of the cohesive components (beam or interface) are assigned with respect to their position, i.e. inside the matrix, inside the aggregate and between aggregate and matrix. With growing model complexity a wide variety of failure features of geomaterials can be represented. Furthermore, the inclusion of an artificial microstructure which regards for stiffer aggregates embedded in a less stiffer matrix enables a coherent quantification of the model.

In a parallel line, adequate homogenization techniques have been introduced since the 1990's. These techniques allow to relate microscopic quantities, like the contact forces and displacements, to corresponding macroscopic quantities, like stresses and strains, compare [8,12,13,15] for a corresponding application to the present DEM model. The development and numerical implementation of adequate homogenization approaches by means of a micro to macro transition from the particle to the macro level supplements the formal definition of the DEM models. Homogenization procedures have been developed which allow for a transfer from a simple Boltzmann continuum based particle model to a more complex continuum with microstructure, see [8] for a detailed overview. However, for brevity no details concerning this topic are given here. Interested readers are referred to the noted literature.

The paper is organized as follows: section 2 provides a brief outline of the theoretical background of a standard (non-cohesive) form of the DEM model supplemented by a discussion on the modeling of cohesion within particle models. In section 4 the extension to an interface enhanced DEM model along with some representative simulation results is sketched. Afterwards, section 5 presents the formulation of a microstructure-based DEM environment which utilizes the interface enhanced model according to section 4. Again, simulation results are used to validate the proposed method. We conclude with a summary of the attained insights and an outlook on future perspectives.

2 Standard DEM model

The starting point of our DEM model development is a two-dimensional DEM code with convex polygonal particles based on the work in [20,21,36]. As this standard DEM model has been presented elsewhere in more detail, see the references above or [8,10,11], the model is only briefly outlined here.

The individual particles can be considered as rigid bodies. They are not breakable and not deformable, but they can overlap when pressed against each other. Three degrees of freedom, two translational and one rotational one, are assigned to each particle center, confer Figure 1a. The local deformational behavior of the particles is approximated by an elastic repulsive force related to the overlapping area of contacting particles, grey shaded in Figure 1a. The contact force is decomposed with respect to the local coordinate system of the contact zone

$$\mathbf{f}^c = f_n^c\,\mathbf{n} + f_t^c\,\mathbf{t}\,. \tag{1}$$

The normal and tangential components of the contact force vector $\mathbf{f}^c$ are defined by

$$\begin{aligned} f_n^c &= -\frac{E_p A_p}{d^c} - m_{\text{eff}}\gamma_n v_{\text{rel},n} \\ f_t^c &= -\min\left(m_{\text{eff}}\gamma_t\left|v_{\text{rel},t}\right|, \mu\left|f_n^c\right|\right)\,. \end{aligned} \tag{2}$$

The coefficients γ_N and γ_T refer to the viscous dissipative damping and μ is chosen according to Coulomb's friction law. Thereby, for $\mu > 0$ the present scheme allows for a non-associated plasticity law, as schematically shown in figure 1b for three characteristic situations. If the grey shaded flow surface is left as for force point ③, the force state is reflected back in vertical direction onto the surface confined by the Coulomb criterion μf_n^c. E_p denotes the elastic modulus of the particles and A_p the overlapping area of two contacting polygons. This overlap represents up to some extent the local (reversible and non-reversible) deformation of the polygons, comparable with the Hertzian contact law for spherical particles. Please note that this representation of the Coulomb friction is a simplification in that the quasistatic limit may not be appropriately captured, since the tangential force tends to zero as the velocity decreases. Alternatively, the tangential

force could be handled via a Cundall–Strack spring, compare [7]. This version has been widely used in the literature, especially in the context of circular particles, because it allows to carry load even if a particle sample, e. g. a heap, is in rest [26]. Since in the present paper the focus lies on polygonal shaped particles that, furthermore, are mostly cohesively bonded together, we believe that the corresponding effect is not so dominant to take it into account. However, future, careful quantitative studies are needed in order to test the validity of the above simplification by comparing simulations with and without friction. A more extensive discussion on the choice of the tangential forces in the context of DEM simulations may for example be found in [4,23]. The relative velocity at the contact zone and the effective mass of two contacting particles i and j are given by

$$\mathbf{v}_{\text{rel}} = \mathbf{v}_j - \mathbf{v}_i \,, \qquad m_{\text{eff}} = \frac{m_i m_j}{m_i + m_j} \,. \tag{3}$$

Since our focus is more on cohesive granular materials than non-cohesive ones, we believe that the rotations of the particles play a subordinate role and, therefore, the angular velocities in equation $(3)_1$ are neglected. The characteristic length of the contact region is defined by $1/d^c = 1/d_i + 1/d_j$, where d_i and d_j define the diameters of circles of equivalent areas as the polygons i and j. The forces and resulting moments are inserted into the equations of motion, which are solved numerically for each particle with the aid of the Gear–Predictor–Corrector time integration scheme, confer [1]. The dynamical basis of the DEM implies the solution of the equation of motion at discrete time steps $t + \Delta t$ for each particle i of all particles N within the sample. Upon definition of $\mathbf{f}_i$ for all interaction forces between two contacting particles and $\mathbf{g}_i$ for the gravitational forces of a particle i, the generalized equation of motion holds for each individual particle i

$$\begin{aligned} &\mathbf{M}_i\, \ddot{\mathbf{x}}_i = \mathbf{f}_i + \mathbf{g}_i \text{ with} \\ &\mathbf{M}_i = \begin{bmatrix} m_i & 0 & 0 \\ 0 & m_i & 0 \\ 0 & 0 & \theta_i \end{bmatrix} \quad \text{and} \quad \mathbf{f}_i = \sum_{j=1}^{n_p} \mathbf{f}_{ij}^p \,. \end{aligned} \tag{4}$$

$\mathbf{M}_i$ represents the diagonal generalized mass matrix and $\ddot{\mathbf{x}}_i$ the generalized acceleration of particle i. m_i describes the mass of polygon i (translational degrees of freedom) and θ_i describes the mass moment of inertia of polygon i (rotational degree of freedom). In the case of a simple (non-cohesive) particle contact $\mathbf{f}_i$ is expressed by equation $(4)_3$, i.e. the generalized interaction force vector $\mathbf{f}_i$ contains solely contact forces. Thus, in the present case it is represented by the generalized particle force vector $\mathbf{f}^p$ which is expressed by $\mathbf{f}^p = \begin{bmatrix} \mathbf{f}^c & m^c \end{bmatrix}^{\mathrm{T}}$ and includes the moment m^c of the contact forces $\mathbf{f}^c$ with respect to the center of mass. Thereby, n_p denotes the number of particle contacts of a particle i. Cohesive forces, as introduced in the coming sections will be simply added on the right hand side of equation $(4)_3$.

The application of this basic (non-cohesive) DEM model has proven to be capable to qualitatively picture the behavior of cohesionless granular materials like sand. The localization of shear bands along with the formation of complex failure pattern was studied by means of dense and porous samples and reflected experimental observations in an astonishing manner. More information on the applied model can be found in [10,11] and descriptive simulation results on cohesionless particle samples can be found in [8,13,15].

3 Modelling of cohesion in particle models

The model presented so far allows for the application to non-cohesive granular materials like sand, stone or rock heaps. Since most geomaterials are more or less cohesive, a model is demanded for which is capable to represent cohesion. In other words, attractive forces between particles are necessary to bond these particles together to some extent. Usually, the physical effect of cohesion is limited for tension. Several ways of incorporating cohesion into particle models are feasible. The implementation strongly depends on the chosen particle shape and problem class. The easiest way in the case of circular particles is the introduction of attractive potentials like in Molecular Dynamics (MD). In this regard, the most prominent law that accounts for attractive action between particles is the Lennard–Jones potential adopted from physical chemistry, see the description in [1]. Another way, only reasonable for circular particles, is based on an extension of the Hertz contact law for "negative" overlaps. An implementation is rather straightforward as the primary geometric variable defining the contact of circles is the distance between the particle centroids, compare [14,24,30,40]. Following this line in [25] an alternative model was proposed where an initial overlap of circular particles accounted for the attracting force law. In contrast to "easy" geometries like circles, the geometric definition of polygonal particles in contact is by far more complex. This is the case as more than one geometric variable describing the contact and the position of the individual bonded edges is involved. The distinction between a point contact (circles) and line contact (polygons) must be drawn. Therefore, alternative options have to be considered. Two different approaches that account for cohesive bonds between two polygon edges have been implemented in the present DEM model: In the first approach beam elements between the centers of mass of neighboring particles are introduced and constitute a beam enhanced DEM model. This approach will not be given in detail here as it was extensively discussed in the past, see [10,11,20,21,22]. The simulation results with a beam enhanced DEM model show that the general failure behavior of cohesive frictional materials like concrete is qualitatively very well represented. In particular, the beam enhanced DEM model is capable to represent typical inherent failure mechanisms of cohesive geomaterials. Furthermore, it has proven to be very well suited for a visualization of these mechanisms which are technically difficult to observe in experiments, [8,10,11]. However, a realistic softening behavior cannot be obtained in simulations with beam enhanced DEM models, due to the presently included breaking law of the beam elements, i.e. the failure appears mostly brittle in the context of normalized load–displace-

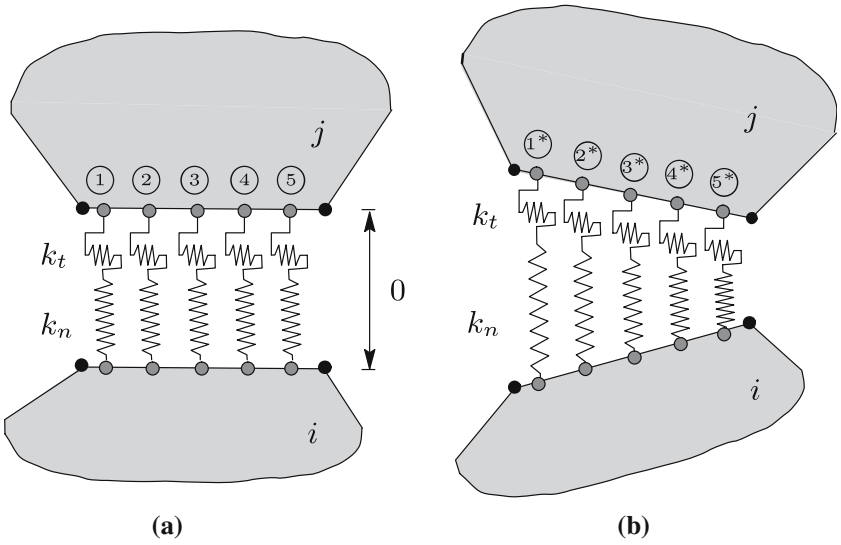

Fig. 2 Idealization of interface in **a** undeformed stage and in **b** deformed stage

ment diagrams. Summarizing, the qualitative picture of the beam enhanced model is satisfactory, but the quantification remains still a demanding task. As an alternative, an interface enhanced DEM model was introduced where continuous interfaces along common particle edges represent the bonding component. The next section is dedicated to this topic.

4 Interface enhanced DEM model

In order to represent the cohesion between particles in a DEM model, an approach borrowed from the Finite Element Methodology (FEM) is adopted. It makes use of so-called interface elements that are directly defined at the particle edges. In that, the model is made more complex: Instead of simple elastic beams with an oversimplified brittle failure law as in earlier versions of this DEM model, see the references in the previous section, more elaborate interface elements with a popular constitutive law on the basis of the plasticity theory are used here. The realization of this interface enhanced model is influenced by a former work of [39] and follows the plasticity formulation introduced therein. The motivation to use this material law in the context of the DEM follows the principle that a proven and established macroscopic material law may be at least much that successful in modeling the failure on a smaller scale as in a continuum model (used typically for a higher scale). Apparently, this approach pictures the real physics involved in the debonding process of bonded granulates far better than the beam enhancing approach.

A variety of models for the representation of the interaction between the constituents of two- and more-phase particle composites via interface elements have been proposed since the late 1960s. The works by [17] and [31] have been pioneering as they were among the first ones to introduce discontinuities into numerical models in the context of the FEM either as continuous or lumped interface elements. On the one hand, lumped interface elements evaluate a force–relative-displacement constitutive relation at a nodal point. Insofar, to a certain extent they exert a similar behavior as simple springs. No further assumptions with regard to tractions and relative displacement distributions across the interfaces are made. On the other hand, the formulation of continuous interface elements (line, plane or shell type) implies a continuous relative displacement field and a traction-relative displacement constitutive relation.

Following these lines interface elements have been the focus of intensive studies in the context of FEM in the past.

4.1 Basic idea

The interface layer is regarded as infinitely thin in the initial stage.Since the particles are undeformable by definition, use is made of the key assumption that the deformation of the interface is constrained to be linear. In analogy to the previously introduced beam model this fact represents the Bernoulli-hypothesis of a planar cross-section to some extent. The interface can be discretized and is represented in a lumped sense by a fixed number of normal and tangential spring sets with stiffnesses k_n and k_t. These springs are attached along the common edge of two initially bonded particles i and j, as shown in Figure 2a. The current location of start and end points of the springs relative to the bond are initially fixed and evaluated after each time step. It is important to note that the interface shown in Figure 2a has a visible initial thickness for visualization reasons only. Ongoing relative motion of the particles leads to a finite value of relative deformation for each spring, i.e. overlapping of particles and, thus, contraction of springs (negative relative deformation) is also allowed. The relative deformation of the bonds is represented by the extension and contraction of the springs, as indicated in Figure 2b.

As further assumption the numerical integration of the constitutive law of the spring sets, which are noted integration points in the sequel, yields an approximated stepwise constant stress distribution over the edge. This procedure compares that for the computation of stress resultants in beams. The constitutive law used throughout this chapter is a non-associated Mohr–Coulomb type softening plasticity model defined by two yield surfaces according to [39] and is discussed in more detail in section 4.2. A failure, or more precisely detachment, of the bonds is achieved, if all integration points of the interface layer are completely softened. It should be kept in mind that no extra contact force according to equation (1) is created, as long as a bond between two particles exists. This means that once the bond is completely detached, a "standard contact" according to section 2 is assumed to control the interaction between two particles. The forces evaluated in the integration points can be combined to a bond force vector and transferred to the mass centers of the involved particles, thus, giving rise to a moment. The bond force vector then takes the form $\mathbf{f}^{\text{bond}} = [f_x^{\text{bond}}\, f_y^{\text{bond}} m^{\text{bond}}]^{\text{T}}$ and enters the equation of motion in (4). The generalized interaction force vector $\mathbf{f}_i$ then takes the form

$$\mathbf{f}_i = \sum_{j=1}^{n_p} \mathbf{f}_{ij}^{p} + \sum_{k=1}^{n_{\text{bond}}} \mathbf{f}_{ik}^{\text{bond}} \,. \tag{5}$$

Additionally to n_p, noting the number of particle contacts of a particle i, n_{bond} denotes the overall number of existing bonds of a particle i.

4.2 Mohr–Coulomb plasticity model

The principal ingredients of a plasticity formulation are the yield condition, the flow rule and the hardening law (if needed), e.g. compare [19]. In the present context the basic idea of a strain-driven formulation from classical plasticity is straightforwardly transferred to a "relative displacement-driven" formulation. The actual state of the spring set is determined by the total relative displacement $\mathbf{u}$, the plastic relative displacement $\mathbf{u}^p$ and the softening variable κ. Here, the range of validity is restricted to small strains and, following the above logic, small relative displacements. Hence, an additive elastic–plastic split of the relative deformation $\mathbf{u}$ of one spring set is admissible

$$\mathbf{u} = \mathbf{u}^e + \mathbf{u}^p \quad \text{with} \quad \mathbf{u} = \begin{bmatrix} u_n \\ u_t \end{bmatrix} . \tag{6}$$

The stress-relative deformation law for the elastic part yields

$$\boldsymbol{\sigma}^{\text{tr}} = \boldsymbol{\sigma}^0 + \mathbf{K}^{\text{bond}} \cdot \mathbf{u} \quad \text{with} \quad \mathbf{K}^{\text{bond}} = \begin{bmatrix} k_n & 0 \\ 0 & k_t \end{bmatrix}, \tag{7}$$

where $\boldsymbol{\sigma}^{tr}$ is the trial stress state, that may lie outside the flow surface f. k_n and k_t represent the normal and tangential spring stiffnesses. The flow rule is denoted by

$$\dot{\mathbf{u}}^p = \dot{\lambda}\, \mathbf{g}(\boldsymbol{\sigma}, \kappa) \tag{8}$$

with the plastic multiplier $\dot{\lambda}$. $\mathbf{g}(\boldsymbol{\sigma}, \kappa)$ represents the direction of the plastic flow, which in the present case is assumed to be non-associated, i.e. the direction of plastic flow is prescribed by the gradient of the plastic potential g in the form $\mathbf{g}(\boldsymbol{\sigma}, \kappa) = \partial g / \partial \boldsymbol{\sigma}$. In general, plastic flow occurs if the yield function $f(\boldsymbol{\sigma}, \kappa)$ and its derivative both vanish: $f = 0$ and $\dot{f} = 0$. The consistency condition $\dot{f} = 0$ then yields

$$\left[\frac{\partial f}{\partial \boldsymbol{\sigma}}\right] \dot{\boldsymbol{\sigma}} - h\dot{\lambda} = 0 \quad \text{with} \quad h = -\left[\frac{\partial f}{\partial \kappa}\right]\left[\frac{\partial \kappa}{\partial \mathbf{u}^p}\right] \cdot \left[\frac{\partial g}{\partial \boldsymbol{\sigma}}\right], \tag{9}$$

where h expresses the hardening parameter. Further elaboration, including a combination of equations (6) to (9) results in a relation between stress and relative displacement rates and, finally, in the corrected stress state $\boldsymbol{\sigma}$ along with the plastic multiplier $\dot{\lambda}$

$$\boldsymbol{\sigma} = \boldsymbol{\sigma}^{\text{tr}} - \underbrace{\frac{f(\boldsymbol{\sigma}^{\text{tr}}, \kappa)}{-\left[\frac{\partial f}{\partial \kappa}\right]\left[\frac{\partial \kappa}{\partial \mathbf{u}^p}\right] \cdot \left[\frac{\partial g}{\partial \boldsymbol{\sigma}}\right] + \left[\frac{\partial f}{\partial \boldsymbol{\sigma}}\right] \cdot \mathbf{K}^{\text{bond}} \cdot \left[\frac{\partial g}{\partial \boldsymbol{\sigma}}\right]}}_{\dot{\lambda}} \mathbf{K}^{\text{bond}} \cdot \left[\frac{\partial g}{\partial \boldsymbol{\sigma}}\right] . \tag{10}$$

The procedure in equation (10) operates as a one-step return mapping algorithm, so that no iteration is needed. However, a simple one-step algorithm that yields an explicit solution for the corrected stress state is only possible if linear yield surfaces, linear plastic potentials and linear softening evolution laws are chosen. The bracket terms in equation (10) are either of scalar or vectorial order.

The initial behavior of the spring sets is assumed to be linear elastic and to depend on the spring constants k_n and k_t. Therefore, no coupling of the springs in the elastic regime is assumed. The softening of a spring set starts when the stress state $\boldsymbol{\sigma} = [\sigma_n \;\; \sigma_t]^{\text{T}}$ reaches the yield surface that in the present context could be viewed as a failure surface. The initial failure surface in the biaxial stress plane is given in Figure 3a by graph ① and is symmetric with respect to the normal stress. Since the failure mechanisms dominated by shear and tension differ substantially in geomaterials, it is advisable to model them separately even on the grain scale. This implies the bounding of the elastic domain by two distinct failure surfaces, usually termed two- or in the general case multi-surface plasticity. Indeed, this does not substantially change the treatment presented above for one single surface, except the singularities in the failure surface at the segue of different failure surface segments, i. e. a unique flow direction cannot be specified. The solution of this problem has been treated by [18] or [2], confer [8] for more details. In analogy to equation (8) the flow rule

$$\dot{\mathbf{u}}^p = \dot{\lambda}_1 \frac{\partial g_1}{\partial \boldsymbol{\sigma}} + \dot{\lambda}_2 \frac{\partial g_2}{\partial \boldsymbol{\sigma}} \tag{11}$$

is adapted to capture the flow directions defined by the two plastic potentials along with the essential constraints $\dot{\lambda}_1 \geq 0$ and $\dot{\lambda}_2 \geq 0$.

In the present case the failure surface resembles a two-surface Mohr–Coulomb type plasticity criterion. The tensile

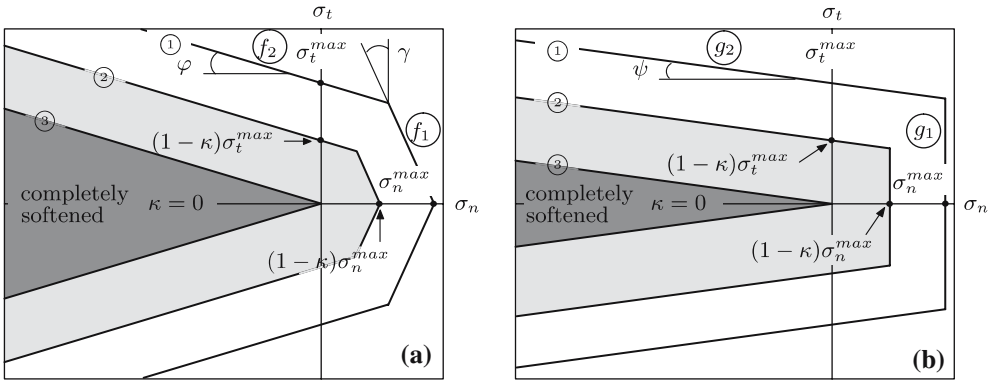

Fig. 3 **a** Failure surface. **b** plastic potential of interface constitutive law in biaxial stress plane

failure is governed by $\sigma_n^{\max} > 0$ and an angle γ which define the yield surface f_1. Whereas the shear failure is controlled by a classical Mohr–Coulomb failure envelope with cohesion $\sigma_t^{\max} > 0$ and friction angle $\varphi > 0$ which define the yield surface f_2. In the compressive regime (for negative σ_n) the trapezoidal or triangle (in the final state) formed by the flow surfaces is open, as no failure is possible in pure compression. With ongoing softening the failure surface shrinks to an intermediate stage (② in Figure 3a) and ends up on the classical Mohr–Coulomb failure surface without any cohesion $\sigma_t = 0$ and tension limit $\sigma_n = 0$, expressed by ③ in Figure 3a. The functional representation of the failure surfaces is given by

$$\begin{aligned} f_1 &= \sigma_n + \sigma_t \tan\gamma - (1-\kappa)\sigma_n^{\max} \leq 0\,, \\ f_2 &= \sigma_n \tan\varphi + \sigma_t - (1-\kappa)\sigma_t^{\max} \leq 0\,. \end{aligned} \tag{12}$$

In order to describe a non-associated plasticity along the lines of the two-surface formulation, two plastic potential surfaces are introduced:

$$\begin{aligned} g_1 &= \sigma_n - (1-\kappa)\sigma_n^{\max} = 0\,, \\ g_2 &= \sigma_n \tan\psi + \sigma_t - (1-\kappa)\sigma_t^{\max} = 0\,. \end{aligned} \tag{13}$$

The plastic potential surfaces are also symmetric with respect to the normal stress, as visualized in Figure 3b.

The softening of the spring set is described by the parameter κ which represents the actual state of damage: κ ranges from 0 in the undamaged state to 1 in the fully damaged state. The softening behavior is driven by the plastic deformation u_n^p and u_t^p of the spring sets in form of predefined fracture energies $G_{f,n}$ and $G_{f,t}$. In the case of a two-surface plasticity this involves two different softening evolutions for tension and shear either, see Figure 4a and b. Pure tensile softening ends after a fracture energy $G_{f,n}$ has been released and pure shear softening ends after a fracture energy $G_{f,t}$ has been released. In the decoupled case, i.e. if only one mechanism is active, the softening variable for the tensile and shear loading is defined by

$$\kappa = \frac{1}{u_n^{\max} - u_n^*} u_n^p\,, \kappa = \frac{1}{u_t^{\max} - u_t^*} u_t^p\,, \tag{14}$$

with $u_n^* = \sigma_n^{\max}/k_n$ and $u_t^* = \sigma_t^{\max}/k_t$, see Figure 4. The plastic part of the deformation starts at u_n^* and u_t^*.

These evolutions are coupled in that, both tensile strength $\sigma_n^{\max}$ and cohesion $\sigma_t^{\max}$ decrease at the same time and at the same rate. This yields an isotropic shrinkage of the failure surfaces, as shown in Figure 3a. A simultaneous tensile and shear softening is treated as linear combination of both, as depicted in Figure 4c. Therefore, the definitions in equation (14) are formally coupled

$$\kappa = \frac{1}{u_n^{\max} - u_n^*} u_n^p + \frac{1}{u_t^{\max} - u_t^*} u_t^p \leq 1\,. \tag{15}$$

By definition, in combined softening u_n^p is solely determined by the plastic deformation due to tensile loading (surface 1 – f_1 and g_1) and not by the normal part of the plastic shear deformation. For this reason, the dilatant behavior with shear loading does not influence the softening since it is physically not justified in combined softening. The predefined fracture energies for mode I and II softening enter the above equations through the integral expression of the graphs in Figure 4a and b. This formalism may be interpreted in the sense of the cohesive crack concept, see e.g. [27], where the crack opening is replaced by the components of the plastic relative displacement. The evolution laws of the normal and tangential stresses

$$\begin{aligned} \sigma_n(u_n^p) &= \sigma_n^{\max}\left(1 - \frac{u_n^p}{u_n^{\max} - u_n^*}\right)\,, \\ \sigma_t(u_t^p) &= \sigma_t^{\max}\left(1 - \frac{u_t^p}{u_t^{\max} - u_t^*}\right)\,, \end{aligned} \tag{16}$$

are inserted into the conditional equations of the fracture energies

$$\begin{aligned} G_{f,n} &= \int_0^{u_n^{\max}-u_n^*} \sigma_n(u_n^p)\,\mathrm{d}u_n^p = \frac{1}{2}\left(u_n^{\max} - u_n^*\right)\sigma_n^{\max}\,, \\ G_{f,t} &= \int_0^{u_t^{\max}-u_t^*} \sigma_t(u_t^p)\,\mathrm{d}u_t^p = \frac{1}{2}\left(u_t^{\max} - u_t^*\right)\sigma_t^{\max}\,. \end{aligned} \tag{17}$$

4.3 Numerical realization

The numerical realization of the plastic interface model in the context of the DEM model is a straightforward task. Each spring set is described by the material law and along each

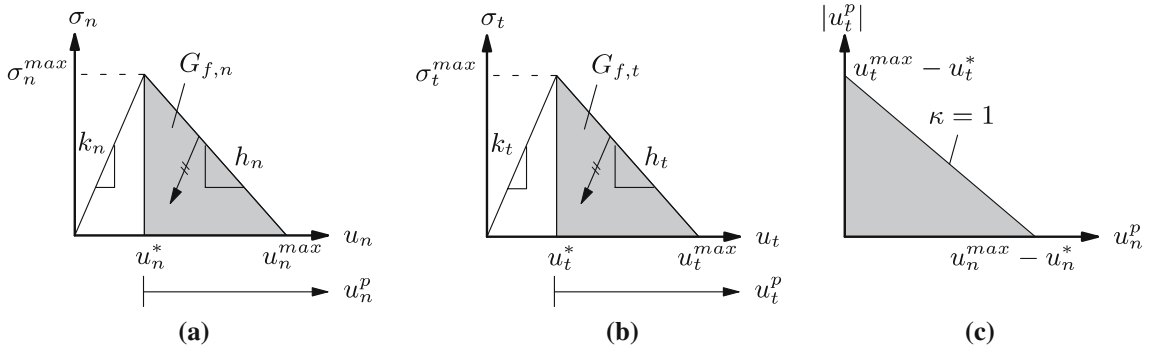

Fig. 4 **a** Evolution law for tensile, **b** shear and **c** combined softening

common edge a fixed number of spring sets, termed integration points, are chosen. From there, it is important to define a reference edge where the corresponding relative displacement-force law is evaluated. Different possibilities are feasible, confer [8,9].

Here, the way displayed in Figure 5 is followed: One bond is chosen as reference edge and the local coordinate system with the normal vector **n** is fixed along this bond. Particle i can be considered as the master and the other one as the slave particle. For this case, the relative deformation of the start and end point of the reference edge are split up into a normal and tangential part. The normal and tangential relative deformation distribution between the start and end point of the reference edge are linearly approximated. The actual complete relative deformation **u** is evaluated at each integration point and is processed in an incremental format $\Delta\mathbf{u}$ by subtracting the complete relative deformations of two successive time steps. The straightforward implementation of the elastic predictor step for the calculation of the trial stress state in equation (7) implies the determination of the spring forces at each integration point k of the bond

$$\begin{aligned} f_{n,k}^{\mathrm{tr}}(\xi) &= \tfrac{1}{n_{ip}} \left[f_{n,k}^{\mathrm{old}}(\xi) + k_n \Delta u_{n,k}(\xi) \right] , \\ f_{t,k}^{\mathrm{tr}}(\xi) &= \tfrac{1}{n_{ip}} \left[f_{t,k}^{\mathrm{old}}(\xi) + k_t \Delta u_{t,k}(\xi) \right] . \end{aligned} \tag{18}$$

n_{ip} denotes the number of integration points along the reference edge and is fixed for all polygon's bonds. The position of the integration point k is determined in the local coordinate system by the normalized coordinate ξ ranging from $[-1, 1]$. In order to evaluate the yield conditions $f_{1/2}(\boldsymbol{\sigma}^{tr}(\xi), \kappa^{\mathrm{old}}(\xi)) \leq 0$ in equation (12) the local stresses at each integration point are computed

$$\sigma_n^{\mathrm{tr}}(\xi) = \frac{f_n^{\mathrm{tr}}(\xi)}{h/n_{ip}}, \quad \sigma_t^{\mathrm{tr}}(\xi) = \frac{f_t^{\mathrm{tr}}(\xi)}{h/n_{ip}} . \tag{19}$$

If the yield surfaces $f_{1/2}$ are left, a plastic corrector step is necessary. Therefore, the type of back projection mode (determination which yield surface/s is/are active) has to be evaluated. Equation (10) yields the corrected stress state at the integration point. Afterwards, an a posteriori check is performed, because it cannot completely be excluded that erroneously a corner regime is predicted, although this is actually not the case. This behavior may appear, as the final position of the yield surface is not known a priori, see [2]. In particular, for stress states in the influence region of the corner a transition from a tensile to a shear state may be obtained. Thereafter, the corresponding forces at the integration points are calculated via an inversion of equation (19). The new forces, the actual relative deformation and the state of softening are saved as history variables for the next time step. All forces along a bond are summed up and transferred to the center of the master particle giving rise to a moment. A force and moment with the same absolute values are applied to the slave particle. An interface is detached or eliminated, if at all integration points of this interface the softening is completed, i.e. $\langle\kappa\rangle = 1$ according to

$$\langle\kappa\rangle = \frac{1}{h} \int_{-1}^{1} \kappa(\xi)\, \mathrm{d}\xi = \frac{1}{n_{ip}} \sum_{k=1}^{n_{ip}} \kappa(\xi_k) . \tag{20}$$

When the softening at all integration points has reached its limit, the bond is detached. For a detailed chart of the interface plasticity law algorithm for one interface with k integration points interested readers are referred to [8]. A standard contact as described in section 2 is assumed whenever two initially bonded particles with broken bond come again into contact.

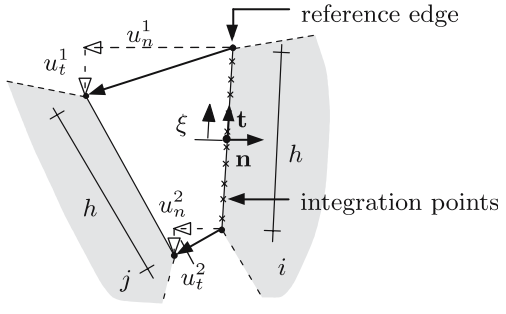

Fig. 5 Numerical integration – Definition of reference edge

4.4 Numerical results

The interface enhanced DEM model is involved in the simulation of standard loading setups. The structured validation

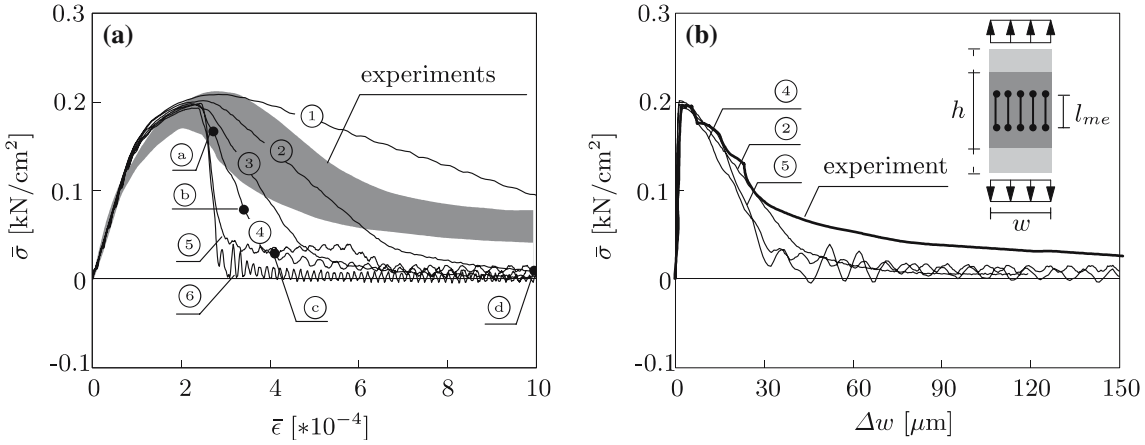

Fig. 6 **a** Stress–strain and **b** stress–displacement diagram of tension test

of this model, first, on the integration point level and, second, by simple loading setups of quadratic rows with a thickness of one particle are presented elsewhere, see [39] and [8]. As these preliminary test programs have been successful, larger samples with variable particle shapes are simulated in uniaxial tension and compression.

4.4.1 Tension simulations

As mentioned earlier, a parameter identification of the beam enhanced DEM model parameters with respect to a quantification of the load-displacement behavior of geomaterials is not convincing at all. The following examples will highlight that the bond description via interfaces is capable to represent the softening not only in very simple tests, as shown before, but also in the context of standard experiments. The softening behavior is investigated by means of a comparative study of rectangular plates with a width of 40 cm and a variable height of 10 cm ①, 20 cm ②, 30 cm ③, 40 cm ④, 64 cm ⑤ and 72 cm ⑥. Thus, the amount of included particles ranges from 400 to 2880. First, the results of a uniaxial tension simulation are presented. The specimens are vertically loaded under constant strain rate conditions by applying the load in a strain driven format via a constant increase of the velocity of the particles at the top and bottom of the plate. Thereby, we follow the procedure firstly described in [33], as it ensures that disturbing initial dynamic effects are reduced to a tolerable level, see the discussion in [22]. The parameters and material properties of the model have been chosen in order to obtain results that are as close as possible to experimental results obtained from the literature. However, only limited information on the "real" values of the bond strength and the corresponding softening behavior is available in the literature. Therefore, no attempt was undertaken to fit the material parameters more closely than needed, since the needed considerable time amount is disproportionate to the additional insight obtained from such a fitting!

Uniaxial tension experiments on concrete by [16] as well as [27] are considered for a quantitative comparison. The normal and tangential stiffness of the interfaces are chosen as $k_n = 1,200\,\mathrm{kN/cm^2}$ and $k_t = 360\,\mathrm{kN/cm^2}$. Moreover, the density was chosen as $\rho = 2.5\,\mathrm{g/cm^3}$ and the time step as $\Delta t = 5 \cdot 10^{-7}\,\mathrm{s}$. The shape parameters of the plasticity model are $\varphi = 26.6°$, $\gamma = 10°$ and $\psi = 0°$, except the maximum yield stress $\sigma_n^{\max} = \sigma_t^{\max} = 0.12\,\mathrm{kN/cm^2}$ and the softening parameters $G_{f,n} = 5.94 \cdot 10^{-4}\,\mathrm{kN/cm^2}$ and $G_{f,t} = 2.98 \cdot 10^{-3}\,\mathrm{kN/cm^2}$. The yield stresses for each interface are statistically distributed around $\pm 10\%$ the average value defined above. Parameters of the contact model according to section 2 like those concerning the viscous damping and friction are set to zero ($\gamma_N = 0$, $\gamma_T = 0$, $\mu = 0$) and the contact stiffness to $E_p = 100\,\mathrm{kN/cm^2}$. The stress-strain curves for the six simulations ① to ⑥ are plotted in Figure 6a along with the experimental results by [16], which are included as a grey shaded band.

It becomes clear that the stress-strain relation is a non-objective measure of the softening, i.e. the longer the specimen the steeper is the post-peak behavior. Nevertheless, the normalized load-displacement relations in Figure 6a generally elucidate the transition from a linear relation to a horizontal tangent up to a complete overall softening of the sample. The stresses are measured in the form of a normalized load as ratio of the reaction force of the boundary particles and the specimen width. The strain is measured via a determination of the ratio of the actual length and the initial length of the specimen. The mesh/length dependence of the strain is one of the main reasons why data of tension tests (of experimental as well as simulation nature) is typically displayed by a stress or load versus. crack width diagram in the literature. The axial deformation is evaluated in a comparable format as in experiments by a measuring device of fixed length $l_{\mathrm{me}} = 5\,\mathrm{cm}$ for all simulations. This means that not the elongation of the complete specimen, but the extension of a fixed area of the specimen containing the macroscopic crack is evaluated. The extension of this fixed area compares to the crack width Δw, see the inset of Figure 6(b). Thus, if a stress–Δw diagram is plotted, all curves coincide and the softening effect is the same regardless of the height of the sample, compare Figure 6b. Moreover, these results have been compared with experimental results in the form of the stress-average-crack

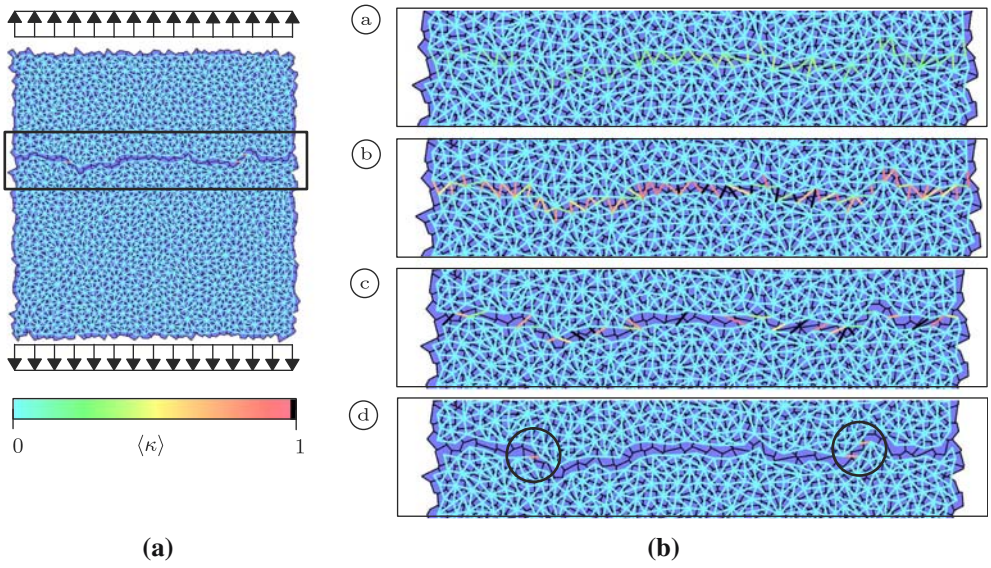

Fig. 7 Simulation output in the post-peak regime: **a** Final stage ⓓ. **b** Detail of macroscopic crack of stages ⓐ to ⓓ

opening diagram of a concrete with a maximum aggregate size $d_{\max} = 1.6\,\text{cm}$ according to Figure 3.49 of [27]. The numerical results fit qualitatively as well as quantitatively well the experimental ones. However, the height of the tail in the softening region could not completely be recast, as the stress drops below the experimental value in the later simulation stages. In the experiments still a considerable stress transfer is obtained in the later softening regime. The reason for this is quite conceivable and can be traced back to the maximum size of aggregates contained within a sample. Moreover, following the discussion in [27] this behavior is an indirect effect of crack face bridging which provides a crack toughening mechanism. In order to enclose the feature of crack face bridging and a corresponding stress transfer even in a later softening stage, one may include a distinct microstructure which for example regards for stiffer aggregates embedded in a less stiffer matrix. This path will be followed in the next section.

An alternative concept takes into account a higher dispersion of bond stiffness and/or yield stresses.

A cutout of the deformed sample ④ in figure 7 at four different time steps ⓐ, ⓑ, ⓒ and ⓓ according to the stress–strain curve in Figure 6a emphasizes the distinct macroscopic crack opening as well as the evolution of softening. The bonds are represented by a line between the respective particles. The scale defines the transition from a non-softening stage to a fully softened stage just before elimination of the bond (black). The state of softening of the bonds $\langle\kappa\rangle$ in Figure 7b is computed based on equation (20) as the average of the softening of all springs (i.e. integration points) representing this bond. One can see that at stage ⓓ the macroscopic crack has completely formed. However, three interfaces positioned perpendicular to the primary load transfer direction (marked by circles) sustain the load and yield a non-vanishing stress of curve ④.

4.4.2 Compression simulations

Next, uniaxial compression tests of plates with different geometries using the same parameter set as for the tension simulation are carried out. Therefore, a similar load setup as discussed before for the tension case but with interchanged loading direction is applied and additionally different boundary conditions are studied. Here, we will discuss the result of a specimen with an unrestricted boundary which represents a situation with very low friction at the boundary. Therefore, the particles forming the upper and lower boundary of the specimen are completely free to move, e.g. like a loading by teflon platens or platens with brushes. For brevity, the stress-strain diagram and a comparison with experimental result is not given, compare [8] for more details. The failure evolution of the unrestricted compression simulation is visualized by means of the output at two time stages ① and ② in Figure 8, which capture the situation around peak load. Once again, the bonds between the particles are represented by a line between them. Time stage ① refers to a situation just before the peak and stage ② to a situation after formation of a failure pattern. The gradual development of inclined localization zones, as shown in Figure 8b has started long before the peak value is reached and yields a sudden breakdown of the particle composite. This result agrees quite well with the experimental results on cubical specimens by [38,39]. However, the softening behavior is less pronounced in compression with respect to the experimental results by Vonk. The simulation output of a restricted sample (high friction case, not given here) resembles the same hourglass failure mode coupled with en-echelon cracks as observed in simulations with the beam enhanced DEM model in [8,10,11] as well as in experiments.

Note that the additional complexity of the bond description compared to the beam one is accompanied by a higher

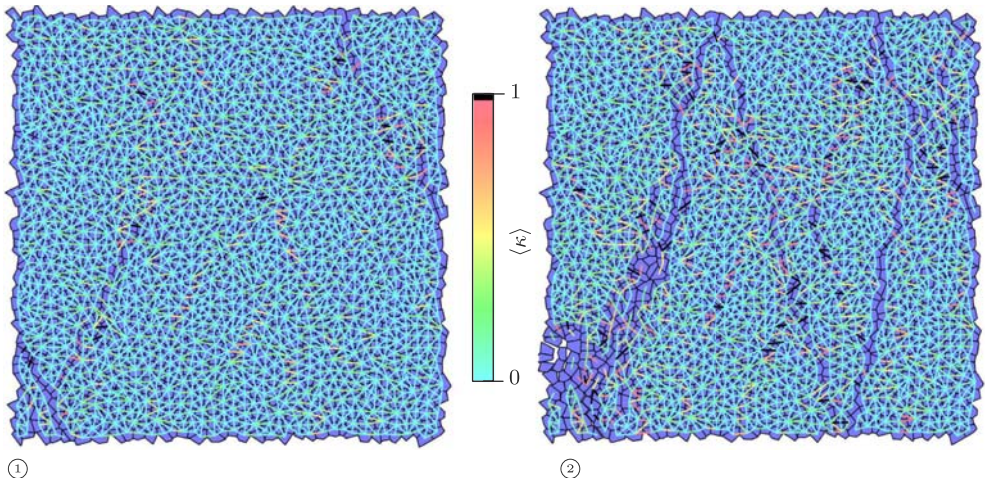

Fig. 8 Failure evolution of compression simulation

sensitivity of the parameter choice with respect to the post-peak failure. This implies that the more or less "controlled" failure in compression as obtained with the beam enhanced DEM model, e.g. compare the results in [8,10,11], is not reproducible with the interface enhanced DEM model in the present form. For example, a continuation of the loading after formation of a failure pattern like that presented in Figure 8 yields a complete disintegration of the initially bonded particle assembly. Thus, no conical rest pieces as in the experiments, e.g. in the form of fragments composed by bonded particles, remain after complete cracking. In the context of this destabilizing effect the following two points are worth to be further investigated: First, the formulation of the interface model has to be enhanced. For example an inclusion of a physical coherent damping or comparable stabilizing contribution to the interface forces may provide for a stable simulation path in the later post-peak regime. Furthermore, a second, probable reason for the found behavior is the missing rotational resistance of two bonded granulates in the interface enhanced model compared to a consideration of it in the beam enhanced model. There, the rotational resistance is considered via the corresponding stiffness entry in the Timoshenko stiffness matrix and the corresponding rotational breaking parameter. The effect of the rotational resistance inherent within the beam enhanced DEM model has already been emphasized as a basic microdeformation mechanism for the simulation of geomaterials by [32].

4.5 Discussion of cohesion modeling

Two approaches that account for cohesion between two polygon edges have been implemented in the context of the DEM model according to section 2. In the first, rather simplistic approach (not presented in detail here) beam elements between the centers of mass of neighboring particles have been introduced, confer [10,11,20,21,22]. As an alternative, a model based on continuous interfaces along common particle edges was proposed in the past section.

The approach based on the introduction of beam elements has shown to be capable to represent most inherent fracture mechanisms of cohesive frictional materials, see the simulation results in [8,10,11]. The simulations fit qualitatively well experimental observations. However, the quantification of the corresponding parameters with respect to the output of experiments like stress-strain curves is still unsatisfactory, confer the discussion in [8]. This is primary due to the choice of the two beam breaking parameters. Although physically plausible from the micromechanical point of view, these parameters cannot be identified with any known (micro) material parameters of geomaterials. Hence, at the present stage, a pure parameter search would end up in a curve fitting without winning any new knowledge on the physics behind it. Anyhow, it should be kept in mind that this model is very well suited for a visualization of typical failure mechanisms appearing in the testing of cohesive geomaterials. The interface enhanced DEM model shows the advantage to picture the real physics involved in the debonding process of bonded granulates far better than the beam enhanced one. However, this is only possible at the expense of a higher computational cost which is required due to the increased complexity of the model and a higher sensitivity of the simulation results with respect to the chosen parameters. The inclusion of the more complex bond representation favors the quantification of the model to experimental results, i.e. the post-peak softening is better reproducible and quantifiable than in the case of the beam enhanced DEM model. Though, still some features like the softening behavior at a later simulation stage in tension as well as a less pronounced softening in compression are to be clarified. Therefore, the complexity of the enhanced DEM model is further enhanced by defining a microstructure-based simulation environment.

5 Microstructure-based DEM model

The inclusion of a microstructure is thought to remedy the mentioned "problem" points. This section comprises simula-

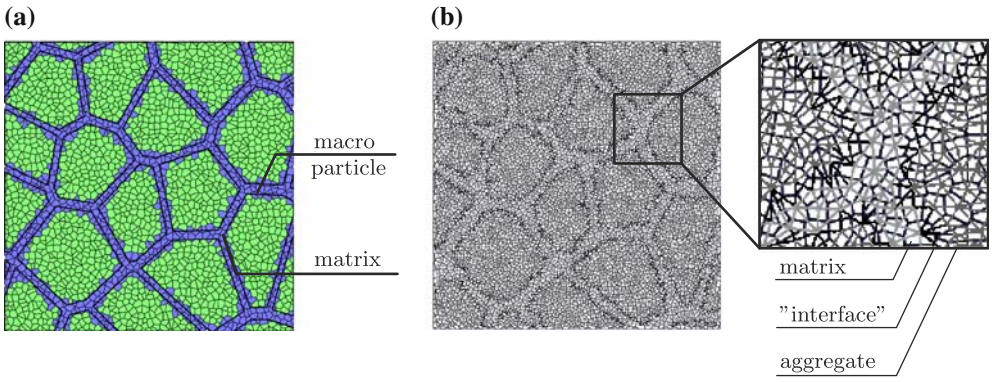

Fig. 9 **a** Definition of particle properties (cohesive components suppressed). **b** Definition of properties of cohesive component

tions with the interface enhanced DEM model where the particle mesh represents an artificial microstructure. Therefore, stiff macro particles that are composed by an agglomeration of a finite number of particles are embedded in a soft matrix, which is also represented by a composition of particles. Insofar, this so-called microstructure-based DEM model may be seen as an extension of the previously introduced interface enhanced DEM model. However, a realization of a microstructure-based simulation environment on the basis of the much simpler beam enhaced DEM method is also conceivable. In order to include a "real" microstructure corresponding digital image processing software has to be connected to the mesh generation module of the DEM program. However, this way is not followed here, since at the present stage an easily realizable implementation is sought. Instead, an alternative, approximative implementation is carried out by creating an "artificial" microstructure, see [8] for more details. In that, the procedures proposed in the framework of the FEM e.g. by [5,35,39] are principally paralleled, as these publications concern the creation of artificial two-phase materials using polygonal aggregate shapes. Furthermore, the present approach is related to that presented in [34], see also [27], where circular aggregate particles are generated based on a statistical distribution which is related to grading curves of concrete. Thus, the composition of a real microstructure of concrete-type materials is treated in an approximate and artificial way here. It is not thought that the simulation results based on a "real" and an "artificial" two-phase microstructure differ that much though. First, the procedure applied for the creation of an artificial microstructure is given. Afterwards, we will present simulation results of uniaxial compression and tension load setups and a concluding discussion of the attained insights.

5.1 Generation of a microstructure

The generation of an artificial microstructure is based on the formulation of macro particles, i.e. one macro particle is composed by an accumulation of a finite number of polygonal particles which are denoted as micro particles. An initially created polygon mesh is overlaid by a mesh composed of larger particles. Certainly, the geometry of a known microstructure, e.g. by means of electron microscopy images, could be included as an overlaying mesh. This option is not considered here, however, is in the realm of possibility in future implementations. After generating a corresponding particle assembly (dense or porous), the particles are scaled down and rotated in a statistical fashion. The scaling down of these (macro) particles by a variable factor is controlled by the desired proportion of aggregate to matrix volume. In order to obtain the overlaying mesh of larger particles the afore mentioned mesh is scaled up. This scaling up depends on the favored size of aggregates. Finally, this mesh is laid over the (underlying) dense particle mesh and represents the pattern for the definition of the macro particles. Based on this information the (micro) particles of the underlying mesh are flagged as being inside or outside the macro particles. The macro particles represent the stiff aggregates and the remaining particles define the matrix. As example the contiguous particles colored in light grey in Figure 9a are identified as the macro particles and the particles colored in dark grey as the matrix material. The corresponding cohesive components are classified as follows, compare also the sketch in Figure 9b: Inside the aggregate (a) (middle grey), inside the matrix (m) (light grey) and defining the "interface layer" between aggregate and matrix (i) (black). This "interface layer" should not be confused with the interface elements used within the interface enhanced DEM model. The first one describes a real material interface layer (between aggregate and matrix), while the last one represents a model interface in form of a component of the enhanced DEM model.

Finally, the values of the stiffnesses of the interface element (k_n, k_t), the corresponding fracture law $(\sigma_n^{\max}, \sigma_t^{\max})$ or both stiffness and fracture law parameters, are chosen accordingly. In order to consider the microstructural properties of a concrete-type material like concrete as best as possible, benefit was made from the extensive knowledge of the group of van Mier. This knowledge comprises the simulation of microstructures via pure beam lattice models starting from the first publication by [34], compare also [27]. The respective parameter ratios between (a), (m) and (i) are estimated based on the corresponding ratios introduced in the context of lattice models. In that, an analogous approach of calibrating

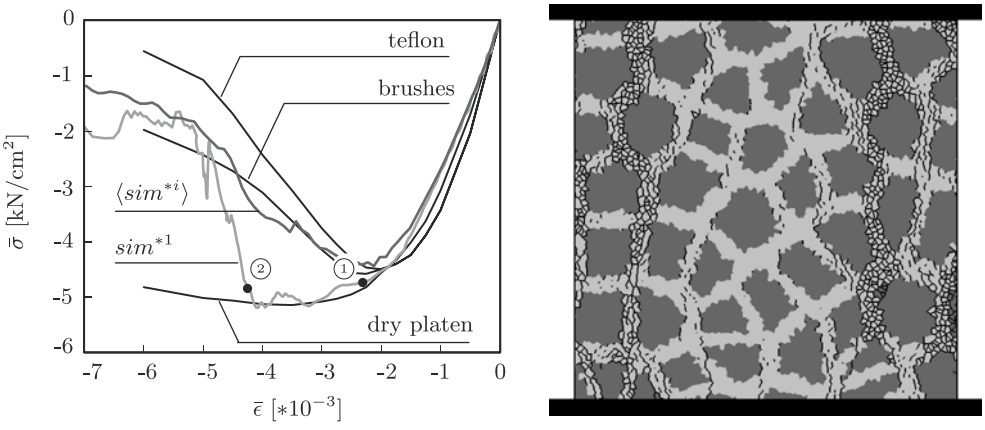

Fig. 10 **a** Stress–strain diagram of simulations and Vonks's experiments. **b** Eliminated bonds at stage ②

the stiffnesses and fracture law parameters noted in [28] is partially followed. In order to prevent aggregate (i.e. macro particle) cracking at the present stage the ratios noted in [28] are partly adopted. The following choices were made:

$$\begin{aligned} \frac{k_n^{(i)}}{k_n^{(m)}} &= 0.1, \quad \frac{k_t^{(i)}}{k_t^{(m)}} = 0.4, \quad \frac{\sigma_{n,t}^{\max,(i)}}{\sigma_{n,t}^{\max,(m)}} = 0.25, \\ \frac{k_n^{(a)}}{k_n^{(m)}} &= 2.8, \quad \frac{k_t^{(a)}}{k_t^{(m)}} = 2.8, \quad \frac{\sigma_{n,t}^{\max,(a)}}{\sigma_{n,t}^{\max,(m)}} = 100. \end{aligned} \tag{21}$$

The matrix values $(\cdot)^m$ are used as input values and the other values, $(\cdot)^a$ and $(\cdot)^i$, result from equation (21). Keep in mind that the choice of parameters is only influenced by the fitting of the softening behavior and without consideration of a detailed, because unknown, knowledge of the "real" micromechanical parameters. Despite the advanced measuring devices and setups available in laboratories, the "real" parameters of the phases (a), (m) and (i) actually remain in the dark, i.e. no precise and experimentally verified values of the phases' stiffness, yield strength and softening law are available. In order to fit experimental results of concrete-type materials these parameters may be estimated on the basis of a macroscopic view of the problem: One supposes that the known macroscopic parameters of concrete are identical to the microscopic ones. For example, the fracture energy of the interface elements is identified as the experimentally measured, macroscopic one and so forth. An alternative and, in the authors opinion, more promising way is the estimation of these parameters on the basis of the insights of section 4 and utilizing the experience of the group of van Mier in the context of the micromechanical simulations of concrete-type materials.

5.2 Numerical results

It is a moot point whether the inclusion of a material description based on an artificial microstructure as introduced in the previous section instead of the "model" material may help to overcome the deficiencies of the beam and interface enhanced DEM models. Recall that the "model" material in section 4 included nearly identical stiffnesses and failure laws of the cohesive components. Compression and tension simulations of an artificial microstructure based on the interface enhanced DEM model presented in section 4 have been carried out. The model parameters have been fit to the compression experiments by [38] under consideration of equation (21).

5.2.1 Compression simulations

The load setup and measuring procedure was already discussed in the context of the tension simulation in section 4.4. Note that the parameter choice is the result of a parameter fitting to experimental results on concrete in absence of more detailed information on the micromechanical parameters. The following matrix parameters have been used: The normal and tangential stiffnesses are chosen as ${k_n}^{(m)} = 2{,}000\,\mathrm{kN/cm^2}$, ${k_t}^{(m)} = 600\,\mathrm{kN/cm^2}$ and the fracture energies as ${G_{f,n}}^{(m)} = 4.996 \cdot 10^{-4}\,\mathrm{kN/cm^2}$, ${G_{f,t}}^{(m)} = 5.988 \cdot 10^{-3}\,\mathrm{kN/cm^2}$. The yield stresses are statistically distributed for each interface about $\pm 10\%$ the average value. On average one gets ${\sigma_n}^{\max,(m)} = 0.04\,\mathrm{kN/cm^2}$, ${\sigma_t}^{\max,(m)} = 0.12\,\mathrm{kN/cm^2}$. Corresponding values for the aggregate and the interface layer between aggregate and matrix are obtained via equation (21). The shape parameters are unaltered with respect to the choice in section 4 and are noted $\varphi = 26.6°$, $\gamma = 10°$ and $\psi = 0°$. The general parameters of the DEM model are also unchanged: The density was chosen as $\rho = 2.5\,\mathrm{g/cm^3}$, the time step as $\Delta t = 5 \cdot 10^{-7}\,\mathrm{s}$, the viscous damping and friction are set to zero ($\gamma_N = 0$, $\gamma_T = 0$, $\mu = 0$) and the contact stiffness amounts to $E_p = 100\,\mathrm{kN/cm^2}$.

Seven compression simulations with the same amount of aggregates and almost identical aggregate/matrix ratios have been carried out. The only difference between these simulation sets is the starting number of the random number generator for the generation of the underlying particle mesh. The quadratic $75 \times 75\,\mathrm{cm^2}$ sample used in simulation

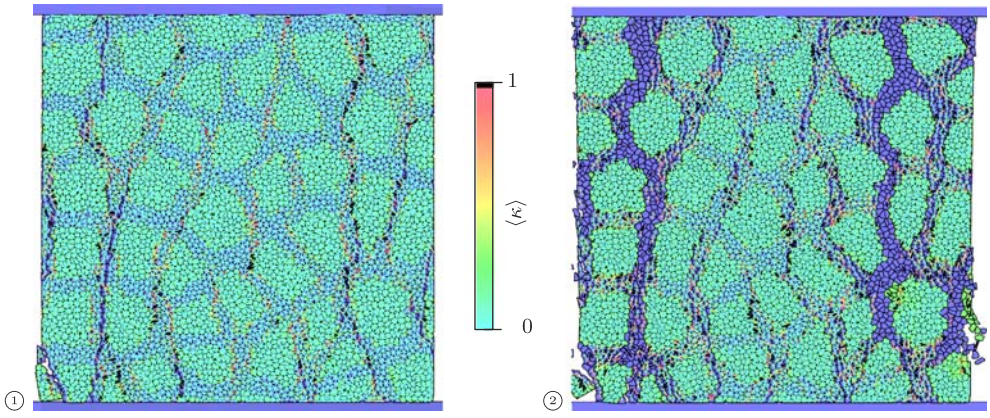

Fig. 11 Graphical output of compression simulation

series sim^{*1} is composed by 5501 particles and a total of 16,489 interface elements between all particles within the sample. The microstructure is created by use of 46 macro particles. The composition of the sample includes a total of 2,896 particles representing the aggregates and a total of 2,605 particles representing the matrix. Thus, the fraction of aggregate volume to complete volume is 0.525. The simulations are confronted with the experiments of [38,39] by means of the nominal stress vs. nominal strain diagram and, in particular, the associated softening branch. The stress-strain curves of all simulation series sim^{*i} with $i = 1, \ldots, 7$ are averaged via a superposition of the corresponding data files. This average curve is symbolically denoted by $\langle sim^{*i} \rangle$. In Figure 10a the comparison of $\langle sim^{*i} \rangle$, simulation series sim^{*1} and Vonk's tests [38] on concrete with different boundary conditions is presented. After linearly increasing in the first part of the loading program the average stress–strain curve $\langle sim^{*i} \rangle$ turns into a non-linear regime up to the peak. Afterwards, in contrast to the simulation results presented in the previous chapters the softening regime is less pronounced, i.e. it follows the predicted experimental results quite well. The continuous failure of interface elements yields a decrease of the stresses with increasing strains. The average simulation result $\langle sim^{*i} \rangle$ lies near the limit curves of the low friction boundary cases (teflon/brushes) in the post-peak regime. In summary, the inclusion of artificial microstructures has proven to be an important feature for a realistic representation of the post-peak softening behavior in terms of the stress-strain relation.

In order to give a detailed view of the failure within the specimen snapshots of simulation series sim^{*1} are considered. The softening stadium of the interface elements is monitored at two time steps ① and ② in Figure 11. These simulation stages document the course of the non-linear and softening branch of curve sim^{*1} in Figure 10a. The simplified picture of the composite structure of the sample in Figure 10b highlights the crack propagation through the specimen shortly after peak load. The dark grey color denotes the aggregate particles and light grey the surrounding matrix. Bear in mind that the aggregates are represented by a finite amount of (macro) particles. For this reason, the shape of the aggregates is irregular. The black lines represent the real geometry of the interface elements that have been eliminated in the course of the simulation, i.e. $\langle \kappa \rangle = 1$. These lines connect the start and end point of an eliminated interface element and represent the corresponding particle edges. The tensile splitting type failure, mostly along the boundaries of the aggregates, is obvious. Two crack zones in the left and right part of the specimen initiate the macroscopic failure of the particle sample. In Figure 11, the brighter background area represents the aggregates, while the darker background displays the matrix. The scale included in this figure refers only to the softening of the interface elements marked by the line connections between bonded particles. Please note that if an interface element reaches a stage $\langle \kappa \rangle > 1$, the corresponding line connection in figure 11 is eliminated. Thus, the dark grey colored matrix particles become visible in regions where the failure localizes, i.e. the overlaying interface element mesh has been partially dissolved in these zones. In the course of simulation at stage ① two macroscopically failure zones form, see Figure 11a. The continuous debonding results in the final failure mechanism in form of a complete disintegration of the matrix material in these zones, compare stage ②, see Figure 11b. The final failure at stage ② pictures the reality quite well, compare the fractured samples by [39].

5.2.2 Tension simulations

The load setup and strain measurement of the tension simulation is accommodated according to section 4.4.

Irrespective of the different material parameters of the target concretes to be compared with, the same DEM parameters as used in the compression simulations are considered in the tension simulations. In tension the experiments by [27] with a concrete with a maximum aggregate size $d_{\max} = 1.6\,\text{cm}$ are considered, compare also Figure 6b. Simulations with different aggregate sizes and varying dispersions of the yield stresses have been performed. The yield stresses have been statistically distributed for each interface element around ± 10, ± 50 and $\pm 90\%$ the average values. The exemplary

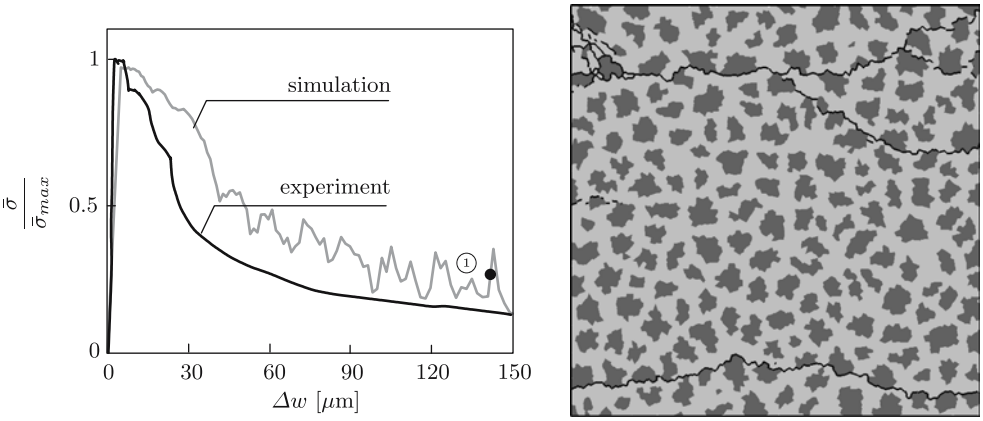

Fig. 12 **a** Stress–displacement diagram of simulations and experiments by van Mier. **b** Eliminated bonds at stage ①

results detailed below are concerned with a simulation series with a dispersion of the yield stresses of ±50% and inclusion of 220 aggregates. Thus, the aggregate size is smaller compared to the compression simulations. Smaller aggregate sizes have been considered to accommodate the smaller maximum aggregate size of the target material in mind. In the context of the realized implementation, the higher the amount of aggregates is chosen, the smaller is the corresponding aggregate size. This yields a higher volume fraction of matrix particles and, finally, a smaller effective stiffness of the composite sample. The $75 \times 75\,\mathrm{cm}^2$ test sample was composed by 2,145 particles representing the aggregates and 3,354 particles representing the matrix. The fraction of aggregate volume to the complete volume amounts to 38.4% and the ratio of aggregate to matrix volume to 0.623.

Figure 12a compares the described simulation series and experimental results of a concrete with a maximum aggregate size $d_{\max} = 1.6\,\mathrm{cm}$ according to [27]. The crack width Δw is measured as difference between the top and bottom particles, since two macroscopically observable cracks appear, see Figure 12b. The sample height is assumed as a representary crack zone with a finite width. The simulated peak stress is less than the experimental one by a factor of 2, if the parameter set of the compression simulation is used.

One reason for this difference is the uncertainty of the parameter choice, since the extraction of "real" parameters from laboratory tests for a definition of the model parameters is not straightforward. Another reason concerns the different target concretes used for the comparisons in the compression and tension simulations. Therefore, the corresponding curves are given in a normalized format by scaling the stresses by the respective maximum stress. Anyhow, the course of the simulated and experimental curves agree qualitatively well. The post-peak behavior is more ductile than predicted by the experiments. Probably, the fracture energy choice was slightly to high. This is not astonishing at all, as the parameters have been pre-optimized for the compression simulations and the corresponding material parameters. As the concrete tested by Vonk differs from that used by van Mier with regard to the different key material parameters, this behavior is quite comprehensible. The snapshot in form of the simplified picture of eliminated interface elements in Figure 12b highlights the crack propagation through the specimen. As expected, only cracks in the horizontal direction and, thus, perpendicular to the loading direction are obtained. The cracks appear mostly at the "interface layer" between aggregate and matrix and fit quite well to the cracking in concrete.

6 Conclusion

Starting from a basic DEM model for non-cohesive polygonal particles, the complexity of the model was successively increased in order to include a coherent representation of cohesive particle assemblies which implied a qualitative as well as quantitative reproduction of characteristic features of cohesive geomaterials. As a quantification of beam enhanced DEM models represents an arduous task, interface elements between the particles have been inserted in order to form a cohesive bond. The last step in the series of increasing complexity was the realization of a microstructure-based simulation environment which utilizes the foregoing enhanced DEM models. With growing intricacy and, therewith, flexibility of the models a wide variety of typical features of cohesive frictional materials could be represented in a satisfactory manner. It was shown that the microstructure-based interface enhanced DEM environment represents an effective approach to remedy the deficiencies of the non-microstructure environments. The inclusion of an artificial microstructure via the definition of corresponding stiffnesses and yield stresses has shown up to be an important feature for a realistic representation of the post-peak softening behavior in terms of the stress–strain relation. With increasing complexity all characteristics of a cohesive frictional material can be represented.

As future perspective, the procedures for a quantification of the parameters should be advanced by further elaborating the relation between the micromechanical properties of geomaterials and the corresponding model parameters. This

implies a consideration of special experimental setups to gain more knowledge on parameters like the micromechanical yield strength or the corresponding ratios for the aggregate, matrix and "interface layer" components. In order to achieve this, very simple composite (model) materials should be created, e.g. regular polygonal particles embedded in a soft matrix with glue between matrix and particles. Due to the clear knowledge of all micromechanical material and, therewith, model parameters, a comparison of simulation and experiment should get much easier. If this point is satisfactorily solved, a real microstructure-based DEM environment may be considered. Then, an interface module between a digital image processing tool that is capable to handle electron microscopy images and the mesh generation module of the DEM program may be incorporated.

Acknowledgements The authors are indebted for the financial support of the German Research Foundation (DFG) within the research group FOR 326 *Modellierung kohäsiver Reibungsmaterialien* under grant no. RA 218/20 . Furthermore, the authors are grateful for the interesting and enlightening discussions with H. J. Herrmann from the University of Stuttgart, Germany, F. Kun from the University of Debrecen, Hungary and S. Luding from Delft University, The Netherlands.

References

1. Allen, M.P., Tildesley, D.J.: Computer simulation of liquids. Oxford University Press, Oxford (1987)
2. de Borst, R.: Integration of plasticity equations for singular yield functions. Comput Struct **26**, 823–829 (1987)
3. de Borst, R., van der Giessen, E.: Material instabilities in solids. Wiley, Chichester (1998)
4. Brendel, L., Dippel, S.: Lasting contacts in molecular dynamics simulations. In: Herrmann, H.J., Hovi, J.P., Luding, S. (eds.) Physics of dry granular materials. vol. 35, pp 313–318. NATO-ASI series E: applied science. Kluwer, Dordrecht (1998)
5. Carol, I., Prat P.C., Lopez, C.M.: Normal/shear cracking model: application to discrete crack analysis. J Eng Mech **123**, 765–773 (1997)
6. Cundall, P.A.: A discontinuous future for numerical modelling in geomechanics. Geotech Eng **149**, 41–47 (2001)
7. Cundall, P.A., Strack O.D.L.: A discrete numerical model for granular assemblages. Géotechnique **29**, 47–65 (1979)
8. D'Addetta, G.A.: Discrete models for cohesive frictional materials. Ph.D. thesis, Bericht Nr. 42, Institut für Baustatik, Universität Stuttgart, Germany (2004)
9. D'Addetta, G.A., Ramm, E.: Discrete modelling of geomaterials. In: Vermeer, P.A., Ehlers, W., Herrmann, H.J., Ramm, E. (eds.) Continuous and discontinuous modelling of cohesive frictional materials – Proceedings of CDM 2004. Balkema, Rotterdam (2004)
10. D'Addetta, G.A., Kun, F., Herrmann, H.J., Ramm, E.: From solids to granulates – discrete element simulations of fracture and fragmentation processes in geomaterials. In: Vermeer, P.A., Diebels, S., Ehlers, W., Herrmann, H.J., Luding, S., Ramm, E. (eds.) Continuous and discontinuous modelling of cohesive frictional materials. Lecture Notes in Physics, vol. 586, pp. 231–258. Springer, Berlin Heidelberg New York (2001)
11. D'Addetta, G.A., Kun, F., Ramm, E.: On the application of a discrete model to the fracture process of cohesive granular materials. Granu Matter **4**, 77–90 (2002)
12. D'Addetta, G.A., Ramm, E., Diebels, S., Ehlers, W.: Homogenization for particle assemblies. In: Cook, B.K., Jensen, R.P. (eds.) Discrete element methods – numerical modeling of discontinua – Proceedings of 3rd international conference on DEM, Santa Fe, NM, USA, Geotechnical Special Publication No. 117, pp. 259–264, ASCE, Reston, VI, USA (2002)
13. D'Addetta, G.A., Ramm, E., Diebels, S., Ehlers, W.: A particle center based homogenization strategy for particle assemblies. Eng Comput **21**, 360–383 (2004)
14. Donzé, F.V., Magnier, S.A. Formulation of a 3-D numerical model of brittle behaviour. Geophys J Int **122**,790–802 (1995)
15. Ehlers, W., Ramm, E., Diebels, S., D'Addetta, G.A.: From particle ensembles to Cosserat continua: homogenization of contact forces towards stresses and couple stresses. Int J Solids Struct **40**, 6681–6702 (2003)
16. Evans, R.H., Marathe, H.S.: Microcracking and stress–strain curves for concrete in tension. Materiaux et constructions **1**, 61–65 (1968)
17. Goodman, R.E., Taylor, R.L., Brekke, T.L.: A model for the mechanics of jointed rock. ASCE J Soil Mech Found Div **94**, 637–659 (1968)
18. Koiter, W.T.: Stress–strain relations, uniqueness and variational theorems for elastic-plastic materials with a singular yield surface. Quart Appl Math **11**, 350–354 (1953)
19. Kuhl, E., D'Addetta, G.A., Herrmann, H.J., Ramm, E.: A comparison of discrete granular material models with continuous microplane formulations. Granul Matter **2**, 113–121 (2000)
20. Kun, F., Herrmann, H.J.: Fragmentation of colliding discs. Int J Mod Phys C **7**, 837–855 (1996)
21. Kun, F., Herrmann, H.J.: A study of fragmentation processes using a discrete element method. Comp Methods Appl Mech Eng **138**, 3–18 (1996)
22. Kun, F., D'Addetta, G.A., Ramm, E., Herrmann. H.J.: Two-dimensional dynamic simulation of fracture and fragmentation of solids. Comp Ass Mech Eng **6**, 385–402 (1999)
23. Luding, S.: Collisions and contacts between two particles. In: Herrmann, H.J., Hovi, J.P., Luding, S. (eds.) Physics of dry granular materials, Vol. 350, pp. 285–304. NATO-ASI series E: applied science Kluwer, Dordrecht (1998)
24. Luding, S.: Micro–macro transition for anisotropic, frictional granular packings. Int J Solids Struct **41**, 5821–5836 (2004)
25. Magnier, S.A., Donzé, F.V.: Numerical simulations of impacts using a discrete element method. Mech Coh Frict Mat **3**, 257–276 (1998)
26. Matuttis, H.G., Luding, S., Herrmann, H.J.: Discrete element simulations of dense packings and heaps made of spherical and non-spherical particles. Powder Technol **109**, 278–292 (2000)
27. van Mier, J.G.M.: Fracture processes of concrete. CRC Press, Boca Raton (1997)
28. van Mier, J.G.M., Schlangen, E., Vervuurt, A., van Vliet, M.R.A.: Damage analysis of brittle disordered materials: concrete and rock. In: Bakker, A. (ed.) Mechanical behaviour of materials. Proceedings of the ICM 7, pp. 101–126. Delft University Press, Delft (1995)
29. Mühlhaus, H.B. (ed.) Continuum models for materials with microstructure. Wiley, Chichester (1995)
30. Mühlhaus, H.B., Sakaguchi, H., Wei, Y.: Particle based modelling of dynamic fracture in jointed rock. In: Yuan (ed.) Procedings of the 9th international conference of the international association of computer methods and advances in geomechanics – IACMAG 97, Wuhan, China, pp 207–216. Balkema, Rotterdam (1997)
31. Ngo, D., Scordelis, A.C.: Finite element analysis of reinforced concrete beams. ACI Mat J **64**, 152–163 (1967)
32. Oda, M., Kazama, H.: Microstructure of shear bands and its relation to the mechanisms of dilatancy and failure of dense granular soils. Géotechnique **48**, 465–481 (1998)
33. Potapov, A.V., Hopkins, M.A., Campbell, C.S.: A two-dimensional dynamic simulation of solid fracture – part II: examples. Int J Mod Phys C **6**, 399–425 (1995)
34. Schlangen, E., van Mier, J.G.M.: Experimental and numerical analysis of micromechanisms of fracture of cement-based composites. Cement Concrete Res **14**, 105–118 (1992)
35. Stankowski, T.: Numerical simulation of progressive failure in particle composites. Ph.D. thesis, University of Colorado, Boulder (1990)

36. Tillemans, H.J., Herrmann, H.J.: Simulating deformations of granular solids under shear. Physica A **217**, 261–288 (1995)
37. Vermeer, P.A., Diebels, S., Ehlers, W., Herrmann, H.J., Luding, S., Ramm, E. (eds.) Continuous and discontinuous modelling of cohesive frictional materials. Lecture Notes in Physics 586. Springer, Berlin Heidelberg Newyork (2001)
38. Vonk, R.: Influence of boundary conditions on softening of concrete loaded in compression. Report TUE/BKO 89.14, Faculteit Bouwkunde, Technische Universiteit Eindhoven, The Netherlands (1989)
39. Vonk, R.: Softening of concrete loaded in compression. Ph.D. thesis, Technische Universiteit Eindhoven, The Netherlands (1992)
40. Zhong, X., Chang, C.S.: Micromechanical modeling for behavior of cementitious granular materials. J Eng Mech **125**, 1280–1285 (1999)